


ARTICLE

Effects of Reduction-Oxidation Cycles on the Structure, Heat and Corrosion Resistance of Haynes 282 Nickel Alloy Manufactured by Using Powder Bed Fusion-Laser Beam Method

Janusz Kamiński¹ | Bogusława Adamczyk-Cieślak¹ | Mateusz Kopec²  | Andrzej Kosiński³ | Ryszard Sitek¹ 

¹Faculty of Materials Science and Engineering, Warsaw University of Technology, Warsaw, Mazowieckie, Poland | ²Laboratory for Materials and Structures Testing, Institute of Fundamental Technological Research Polish Academy of Sciences, Warsaw, Mazowieckie, Poland | ³Laboratory of Surface Analysis, Institute of Physical Chemistry Polish Academy of Sciences, Warsaw, Mazowieckie, Poland

Correspondence: Ryszard Sitek (ryszard.sitek@pw.edu.pl)

Received: 16 May 2024 | **Revised:** 8 October 2024 | **Accepted:** 20 October 2024

Funding: The research was funded by POB Technologie Materiałowe of Warsaw University of Technology within the Excellence Initiative: Research University (IDUB) programme.

Keywords: corrosion | DMLS | haynes 282 nickel superalloy | hydrogen | oxidation

ABSTRACT

The study investigated the effect of the oxidation–reduction cycles on the structure and corrosion resistance of the Haynes 282 nickel superalloy at ambient and elevated temperatures. The comparative studies were performed on specimens produced by the Powder Bed Fusion-Laser Beam (PBF-LB) process and those in the as-received state. The microstructure of the PBF-LB specimens was studied using optical and scanning electron microscopy, whereas the chemical composition of the scale formed after isothermal oxidation in an air atmosphere at 750°C was analysed using energy-dispersive X-ray spectroscopy and X-ray Photoelectron Spectroscopy. The phase composition of the formed scale was determined by X-ray diffraction. Laboratory-induced hydrogen atmosphere was adopted through cathodic charging. A comparison of corrosion resistance was carried out on two types of Haynes 282 specimens, before and after the oxidation and cathodic charging processes. It was found that PBF-LB process could be effectively used to manufacture Haynes 282 nickel superalloy with low porosity and a fine crystalline microstructure. The low-porous, fine-crystalline microstructure of the tested specimens produced by the PBF-LB technique exhibited good resistance to electrochemical corrosion, slightly lower than wrought Haynes 282 nickel superalloy specimens.

1 | Introduction

Nickel superalloys are widely used in various industries (including energy, aviation, oil and gas processing) [1–3]. Such a wide range of applications is due to their excellent mechanical properties, resistance to oxidation at high temperatures and resistance to electrochemical corrosion in many environments [4, 5]. A spontaneously formed passive oxide layer on the surface significantly increases the corrosion resistance as compared to the active state. However, it accelerates the material's susceptibility to local

corrosion in the presence of aggressive ions (Cl^- , SO_4) [6]. In many industrial environments, a frequently observed threat that reduces the durability of materials is a high concentration of hydrogen [7]. It is directly related to the sensitivity of nickel superalloys to the presence of hydrogen in the environment and the subsequent growth of strengthening phases γ' and γ'' formed in the matrix during the ageing process. Also, secondary phases, including the δ phase (Ni_3Nb), the η phase (Ni_3Ti), the σ phase/F phase and various carbides, and carbonitrides might be the places of initiation of trans or intergranular cracks under hydrogen

occlusion conditions [8]. The volume of these phases depends on the chemical composition and the heat treatment used; therefore, different nickel-based superalloys exhibit various heat resistance.

In the aviation industry, nickel superalloys are used, among others, as blade elements in aircraft engines. When the engine is running, an oxide scale is formed on its surface, and when the engine is stopped, condensed components of aviation fuels may be deposited. Furthermore, accelerated degradation of the resulting oxide scale may occur when these structural elements are exposed to long-term immobilisation, especially in coastal atmospheres rich in chloride ions. The oxidation-reduction cycles proposed in the methodology partially reflect such environmental conditions. One of the recent nickel superalloys developed for high-temperature applications in aggressive environments is the Haynes 282 nickel superalloy. However, Haynes 282 exhibits extreme hydrogen embrittlement, resulting in a drastic decrease in both strength and ductility [9] due to the coexistence of strengthening phases γ' -Ni₃Al and carbides (MC, M₆C, M₂₃C₆) in the presence of hydrogen. In recent years, the powder bed fusion (PBF) methods, for example, selective laser melting (SLM) or direct metal laser sintering (DMLS), are increasingly adopted in the production of metallic parts from various alloys, such as Ni-based superalloys, stainless steels or titanium alloys [10–13]. These processes offer many advantages over conventional manufacturing methods (e.g., it is possible to design complex freeform geometries, internal features and challenging internal passages). However, the manufactured components may exhibit some negative material features, including nonequilibrium microstructures, residual stresses, or anisotropic properties. These effects appear during the building of the net-shaped parts with complex geometries and can be reduced by the proper selection of process parameters [14–16]. On the other hand, material anisotropy can be reduced during heat treatment [17].

Haynes 282 alloy's potential application in power plants has led to considerable interest in its oxidation behaviour and corrosion resistance at elevated temperatures. Research on isothermal oxidation has shown that the oxidation kinetics of the alloy obey a parabolic or linear/quasi-parabolic kinetic law in the range of the temperatures studied [18–20]. Depending on the oxidising atmosphere, the main components of the growth oxide layer include phases such as TiO₂, Cr₂O₃, Al₂O₃, MnTiO₃ and MnCr₂O₄, while complex structures with distinctive internal and external oxidation layers are often formed [21–23]. Numerous studies have been carried out on the durability of oxide scale in various corrosive atmospheres [24–27]. Research by Ko et al. indicates that grain refinement can promote resistance to the long-term oxidation of Haynes 282, despite the depletion of Cr in the initial stages of the process [28]. Good corrosion resistance and the formation of a compact passive layer were observed during exposure of Haynes 282 to hydrochloric acid at ambient temperature [6]. All of these literature reports concerned the cast Haynes 282 alloy. In the case of

materials manufactured using additive technologies, literature data are significantly limited.

Therefore, the aim of the work was to investigate the corrosion resistance of oxide scale in subsequent reduction-oxidation cycles of Haynes 282 additively manufactured by using the DMLS process. Additionally, the impact of saturating the substrate with cathodic hydrogen on the early stages of high-temperature oxidation was studied.

2 | Materials and Methods

2.1 | Specimen Preparation

The research compared two types of Haynes 282 nickel superalloy: conventional HY282 (hereinafter referred to as HY282), produced via conventional methods and cut from a rod and HY282-DMLS (hereinafter HY282-DMLS) fabricated using DMLS technology.

The Amperprint0233 Haynes 282 powder purchased from Höganäs company (German) (HY282-DMLS) was used to manufacture specimens of 20 × 20 × 10 mm. The conventional specimens (HY282), for comparative purposes were cut from a 30 mm diameter rod. The chemical composition of the powder and rod is given in Table 1. The nominal diameter of the spherical particles ranges between 15 and 45 μm. Specimens for research HY282-DMLS were produced using an EOS M 100 printer (Germany) operating in the DMLS technology, belonging to the Powder Bed Fusion method. The printer was equipped with a 200 W fibre laser. The process parameters were optimised in the previous paper [29].

2.2 | Reduction-Oxidation Cycles

Both HY282-DMLS and HY282 were subjected to cyclic reduction/oxidation processes. Individual H-O cycles began with saturating the substrate with cathodic hydrogen (during 60 min), and then, on such defective substrates, an isothermal oxidation process lasting many hours (24 h) was carried out. In subsequent cycles, the mentioned processes were repeated several times (1 ×–6 ×). The diagram of the processes used is presented in Figure 1. Additionally, single oxidation (1 × O) or hydrogen saturation (1 × H) processes were performed to illustrate changes in microstructure and corrosion resistance in the initial stages of the project.

2.2.1 | Cathodic Hydrogen Charging

Oxidised and nonoxidised samples were charged with hydrogen to assess their resistance to hydrogen embrittlement, a crucial

TABLE 1 | Chemical composition of Haynes 282 nickel and its powder (% wt.).

	Ni	Cr	Co	Mo	Ti	Al	Fe	Mg	Si	C	B
Powder	bal.	19.5	10.0	8.5	2.1	1.5	1.5	0.3	0.15	0.05	0.005
Conventional	bal.	20.0	10.0	8.5	2.1	1.5	1.5	0.3	0.15	0.06	0.006

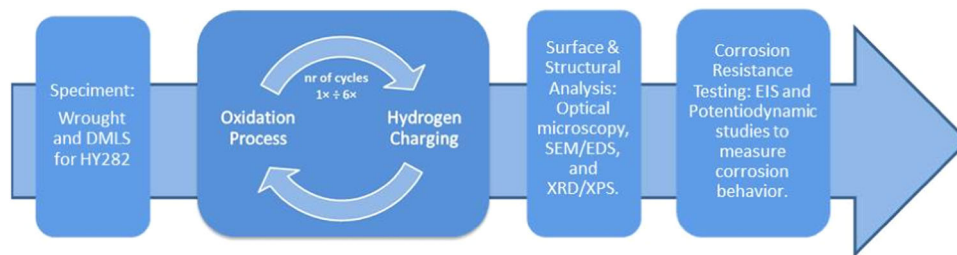


FIGURE 1 | Schematic graph of the methodology used. [Color figure can be viewed at wileyonlinelibrary.com]

factor in assessing the suitability of materials for long-term high-temperature applications where hydrogen-induced damage can occur. Hydrogen was introduced by cathodic charging at 0.05 A/cm^2 at room temperature for 1 h (single cycle time) in a $0.5 \text{ M H}_2\text{SO}_4$ solution with $1 \text{ mg of As}_2\text{O}_3$ per 1 dm^3 as a hydrogen entry promoter. This method accelerates degradation, enabling the study of material stability.

2.2.2 | Isothermal Oxidation

Both HY282-DMLS and HY282 were subjected to oxidation processes. Isothermal oxidation processes were carried out in an air atmosphere at a temperature of 750°C for 24 h (one cycle time) using a heat treatment furnace from Czylok (FCF 16/160 M Polska). The tested materials were heated to a temperature of 750°C at a rate of 100°C/min , and the cooling process was carried out in an air atmosphere in the furnace.

The purpose of performing isothermal oxidation was to investigate how the materials behave under high-temperature oxidative conditions. Six 24-h cycles were chosen to simulate long-term oxidation, and observations were made after both the first and last cycles.

2.3 | Microstructural Analysis

After oxidation, samples were etched using Kalling's 2 reagent to reveal the microstructure. The microstructure was observed using a Zeiss Axio Scope optical microscope (Carl Zeiss Microscopy GmbH, Jena, Germany). This allowed for the examination of grain boundaries, phase distributions, and defects introduced by the DMLS process or oxidative damage.

2.4 | Chemical and Phase Composition

To further analyse surface morphology and chemical composition of the oxide scales, a Scanning Electron Microscope (Hitachi SU8000, High-Tech. Corp., Tokyo, Japan) with secondary electron (SE) and backscattered electron (BSE) modes, along with energy dispersive X-ray spectroscopy (EDS), was used. EDS allowed for elemental mapping of the oxide scales, revealing the distribution of key elements like nickel and chromium.

To characterise the crystallographic structure of the oxide scales formed during oxidation, XRD measurements were carried out. The identification of phases formed (like oxides of nickel and

chromium) was crucial for understanding the oxidation mechanisms and the role of protective oxide layers in enhancing corrosion resistance.

X-ray diffraction has been carried out on a Bruker D8 Advance diffractometer (Bruker Corp., Billerica, MA, USA) (goniometer radius 280 mm), equipped with parallel beam optics and a $\text{Cu K}\alpha$ radiation ($\lambda = 0.154056 \text{ nm}$) source that operates at 40 kV and 40 mA . The scan optics are a Göbel mirror on the incident beam side and twin secondary Soller slits in the diffracted beam. The measurements were performed with a fixed angle of incidence of the primary beam equal to 2° , over the 2θ range between 20° and 100° , with a step size of 0.05° and 5 s counting time per step. X-ray diffraction (XRD) patterns were analysed using Bruker EVA software (V3.0) and the PDF-2 database (from the International Centre for Diffraction Data).

Complementary to EDS, XPS was used for detailed chemical analysis of surface oxide layers, providing more precise information about the oxidation state and composition of elements like nickel, chromium, and oxygen.

XPS analysis of the tested materials was performed using X-ray photoelectron spectroscopy measurements using a Microlab 350 spectrometer (Thermo Scientific, Waltham, USA) at an excitation energy of 1456.6 eV . The recorded spectra were deconvoluted using the asymmetric Gauss/Lorentz function in the Thermo Avantage software version 5.9911 to determine the chemical state of the detected elements and the chemical composition of the tested surfaces.

2.5 | Corrosion Test

Corrosion resistance tests of the Haynes 282 nickel superalloy (produced using conventional technology—HY282) and using the DMLS method (HY282-DMLS), in the initial state and after the hydrogen charging/oxidation processes, were performed using impedance spectroscopy (EIS) and the potentiodynamic (LSV) method on an AutoLab PGSTAT100 (AutoLab, Eco-Chemie B.V, Utrecht, Netherlands) in a nondeoxygenated solution of $0.1 \text{ M Na}_2\text{SO}_4 + 0.1 \text{ M NaCl}$ at ambient temperature. Before the electrochemical testing, the specimens were exposed to a corrosion solution under current-free conditions for 3600 s , as required to stabilise the open-circuit potential. The EIS measurements were conducted in a three-electrode system (working electrode—reference electrode ([saturated calomel electrode SCE])—counter electrode [platinum]) in a

frequency range of 10^5 – 10^{-3} Hz, with a sinusoidal signal amplitude of 10 mV in potentiostatic mode at the open circuit potential (E_{OCP}). The electrochemical studies were conducted using a Faraday cage. Impedance spectra were analysed using Baukamp's EQUIVCRT programme. In the case of the initial material, an equivalent circuit (EC) with a one-time constant was used. Increasing the number of time constants was caused by the increasing electrochemical nonhomogeneity of the substrate as the number of oxidation-reduction cycles increased. Equivalent circuits used R(Q[R(RQ)]) or R(RQ)(Q[R(RQ)]) are commonly used for materials prone to localised corrosion. The resulting spectra were presented as Bode plots. The method provides insights into the electrochemical properties of the oxide layers formed during oxidation cycles. Using impedance spectroscopy (EIS) helps identify localised corrosion or other degradation mechanisms in the surface layers by measuring changes in resistance and capacitance.

Potentiodynamic studies were carried out in an identical three-electrode system up to a potential of 1500 mV. The material was polarised with a potential increase rate of 0.2 mV/s. The slow potential sweep rate allowed for a precise understanding of how the materials behaved in a corrosive environment. Polarisation resistance data provided insights into the corrosion current and passivation behaviour.

3 | Results and Discussion

3.1 | Microstructure

Figure 2 shows images of the microstructure of Haynes 282 in the initial state and HY282-DMLS obtained in the XY-direction plane. The microstructure of HY282 (Figure 2a) is formed of austenite grains and twins. As shown in Figure 2b, the microstructure of Haynes 282 alloy after the DMLS process consists of characteristic layers of welding pools.

A different microstructure in the XYZ directions translates into a high anisotropy of functional properties commonly observed in materials manufactured using additive technologies [30]. In this work, electrochemical tests were carried out using surfaces in the XY directions.

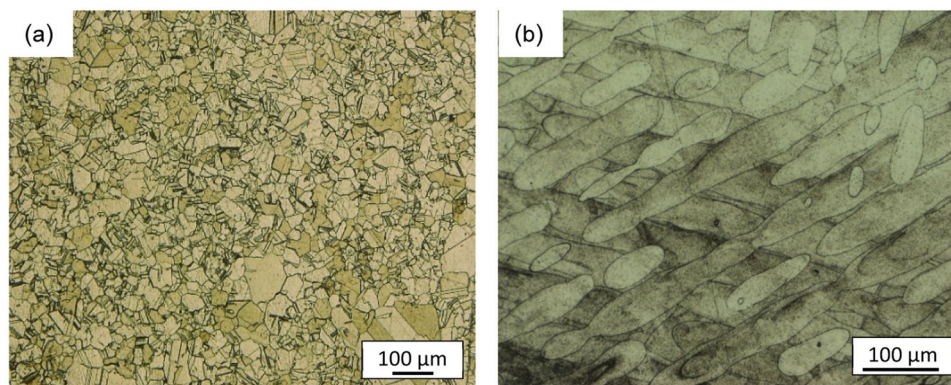


FIGURE 2 | Microstructure of HY282 in the initial state (a) and HY282-DMLS (b) in the plane perpendicular to the building direction (XY). [Color figure can be viewed at wileyonlinelibrary.com]

3.2 | Oxidation

The oxidation of nickel superalloys results in the formation of a multiphase scale. Depending on the chemical composition of the substrate and the oxidising atmosphere, different types of oxides are observed in the scale: NiO, Al_2O_3 , Cr_2O_3 and TiO_2 . In the case of nickel superalloy HY282, whose chromium content is less than 25% wt., in addition to Cr_2O_3 small amounts of $\text{NiO}^*\text{Cr}_2\text{O}_3$ spinel and titanium oxides are often observed on the outer surface of the scale [22]. The formed Cr_2O_3 chromium oxide layer protects the substrate from further oxidation. Simultaneously, the nonhomogeneity of the scale (especially in the case of additive technologies) allows oxygen to diffuse across grain boundaries and increase internal oxidation, which is commonly observed for nickel or cobalt alloys. The internal oxide consists of Al_2O_3 and TiO_2 phases, which are formed from gamma-prime (γ') strengthened alloy ($\text{Ni}_3(\text{Ti}, \text{Al})$ phase) [31]. The available literature [22] shows that a parabolic oxidation mechanism occurs in the HY282 nickel alloy, causing a reduction in the corrosion rate in subsequent cycles. Regardless of the morphology of the oxide layer, it is possible for oxygen to diffuse across grain boundaries, allowing internal oxidation to occur, especially when a defective oxygen scale is formed during cathodic hydrogen charging.

After a 24-h oxidation process at 750°C (Figure 3a,b), the presence of internal oxidation was observed in HY282 nickel alloy produced by the DMLS technique. The conducted EDS tests showed that the light bands observed in Figure 3b are areas of depletion of the substrate from elements undergoing internal oxidation, that is, Al and Ti, the high concentration of which is observed immediately below the zone of chromium oxides. Due to multiple cathodic hydrogenations, the oxide scale formed is damaged to facilitate internal oxidation (Figure 3c,d).

In the case of the HY282-DMLS, the thickness of the oxide scale is comparable in all H-O cycles and is approximately 1 μm, with increasing areas of internal oxidation in subsequent cycles.

In the case of the HY282 (Figure 4), short-term (24 h) oxidation (750°C) occurred mainly at the grain boundaries. As a result of extending the oxidation time, the thickness of the oxide scale increases from ~0.5 to ~3 μm after six cycles of HO. The effect of hydrogen on the structure and, indirectly, on oxidation resistance is observed during the initial stages of oxidation.

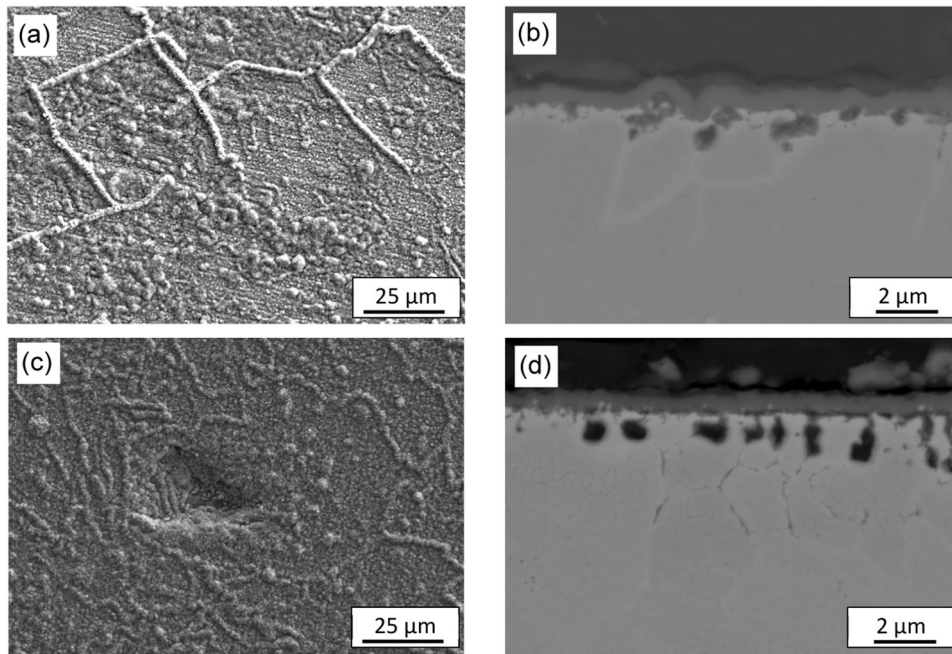


FIGURE 3 | Surface morphology (a, c) and microstructure (b, d) of the oxide scale formed after (a, b) 24 h of oxidation; (c, d) 6 × HO cycles on HY282-DMLS nickel alloy. [Color figure can be viewed at wileyonlinelibrary.com]

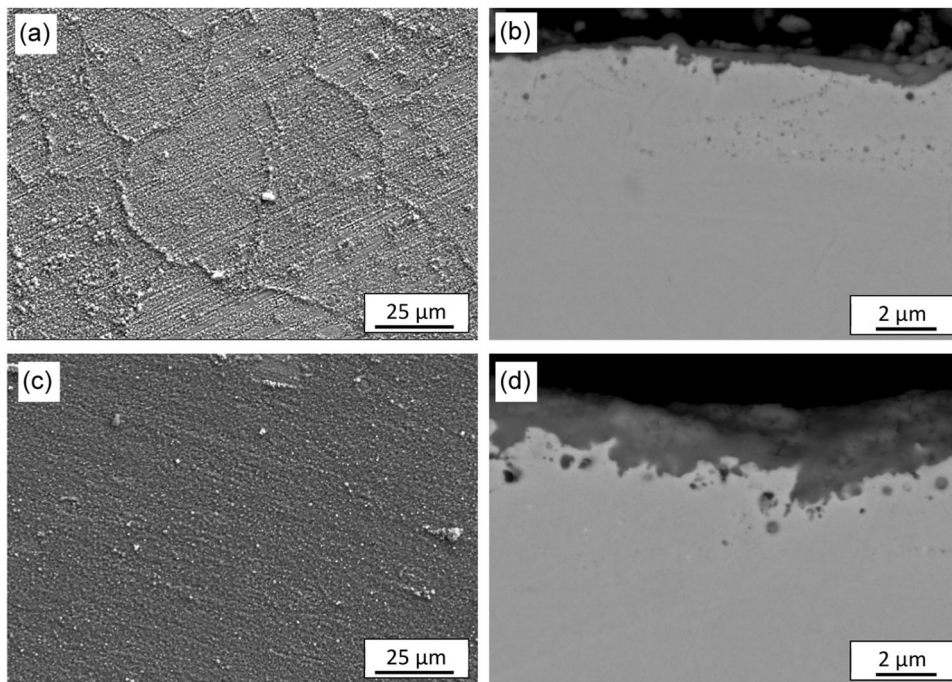


FIGURE 4 | Surface morphology (a, c) and microstructure (b, d) of the oxide scale formed after: (a, b) 24 h of oxidation; (c, d) 6 × HO cycles on HY282 nickel alloy in initial state. [Color figure can be viewed at wileyonlinelibrary.com]

The material subjected to cathodic hydrogenation exhibits numerous longitudinal–transverse cracks; this is particularly noticeable in the case of materials after additive manufacturing (Figure 5a). In the case of the HY282 in its initial state, the influence of hydrogen (50 mA/cm² for 60 min) on the presence of defects in the structure is negligible (Figure 5b).

This phenomenon is confirmed by the comparable electrochemical parameters and the shape of the potentiodynamic

curves of the specimens after oxidation, and after hydrogenation and oxidation, as described later in this study. The result proves that, through the introduction of defects or cracks, the oxidation of the material is accelerated. This fact is consistent with the available literature data [32] reporting a positive correlation between roughness and oxidation intensity. It was found that the larger the contact area between the oxidant and the metallic material, the faster the possible adsorption of the oxidant, whereby the initial stages of surface oxidation are

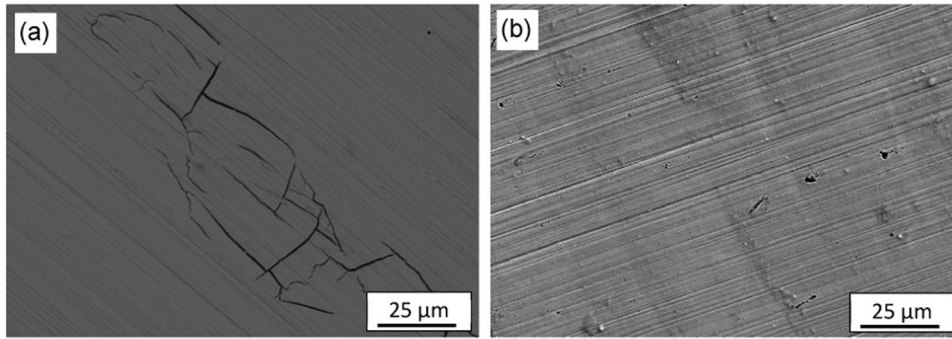


FIGURE 5 | Surface morphology of HY282 nickel alloy after 60 min hydrogen-charged 50 mA/cm² (a) HY282-DMLS and (b) HY282 in initial state. [Color figure can be viewed at wileyonlinelibrary.com]

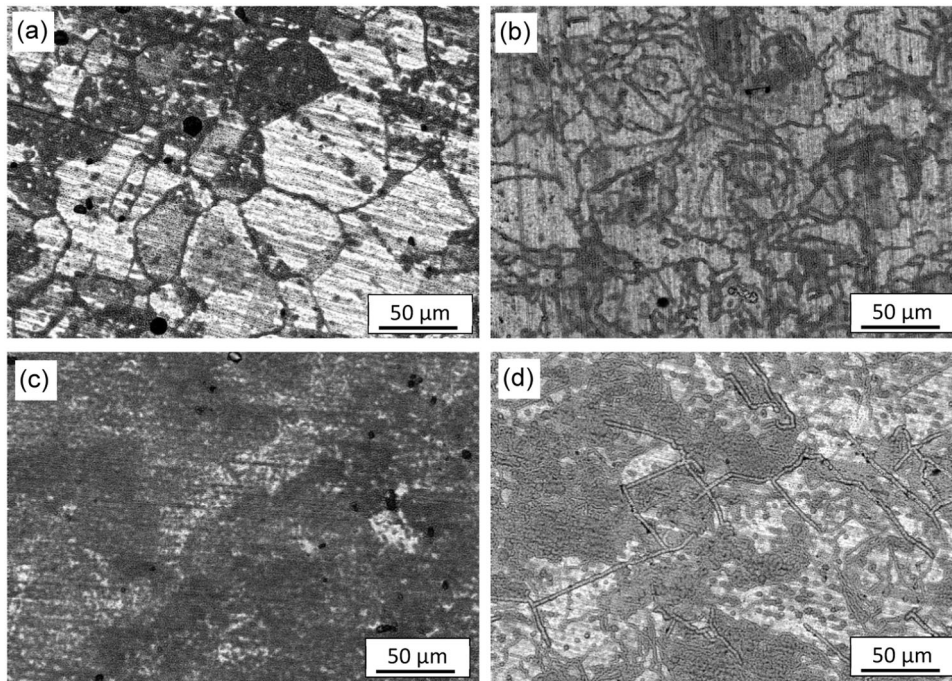


FIGURE 6 | Surface topography of Haynes 282 nickel alloy specimens: (a) HY282 in initial state after 24 h oxidation (1×O); (b) HY282-DMLS after 24 h oxidation (1×O); (c) HY282 in initial state after one cycle of cathodic hydrogen saturation and one oxidation cycle (1×HO); (d) HY282-DMLS, after one cycle of cathodic hydrogen saturation and one oxidation cycle (1×HO). [Color figure can be viewed at wileyonlinelibrary.com]

intensified. In the case of single oxidation of the HY282 nickel alloy (Figure 6a), the oxidation process occurred mainly along grain boundaries and in grains that displayed increased surface energy. Figure 6c,d presents the surface topography after 24 h of oxidation following prior saturation of the surface with hydrogen (1×HO). In the case of the conventional material, a relatively homogeneous, thin oxide scale forms. In the case of the DMLS material, the oxide layer is noticeably chemically heterogeneous. Grains are observed with high variability in crystallographic orientation, which causes significant anisotropy in the formation of oxide phase nuclei, and thus causes differences in the thickness of the oxide layer, which favours the formation of the so-called ‘whiskers’, that is oxides in the form of thin, long needles growing perpendicular to the substrate material [33]. In the additively manufactured material, the high electrochemical nonhomogeneity of the oxide layer that results from the above-mentioned variation in the thickness of the scale causes a decrease in the substrate’s corrosion resistance.

3.3 | Chemical and Phase Composition

The change in the corrosion resistance of HY282 nickel alloy observed in subsequent cycles is determined by a number of factors, such as the initial microstructure, the presence of hydrogen, exfoliating the oxide scale caused by an increase in residual stress as a result of the increase in the size of NiCrO₄ precipitates [34] and the formation of Ni-Co precipitates on the surface (Figures 7 and 8). Depending on the Ni/Co ratio, these areas can have contradictory effects on corrosion resistance. Studies by Srivastava et al. [35] and Bakhit et al. [36] showed that Ni-20Co coatings had the best corrosion resistance, probably due to the presence of the fcc phase. Increasing the amount of cobalt significantly decreased the corrosion resistance due to the formation of the hcp phase or a mixture of hcp + fcc phases. Similar results were obtained in the present study; cobalt-containing precipitates in a range of 19%–24% Co were almost stable during the potentiodynamic

tests, compared with Ni50–Co50 precipitates, which underwent significant degradation.

The increase in the volume of Ni-Co precipitates caused the formation of aluminium clusters (up to about 5.6% wt), which may cause the dissolution of these areas in an acidic medium due to the amphoteric nature of aluminium. In addition, the presence of sulphates in the fuel can cause the formation of water-soluble aluminium sulphates with the formation of $\text{Al}_2(\text{SO}_4)_3 \cdot 16\text{H}_2\text{O}$ hydrates.

The changes that occur in the surface topography of the oxide layers during the reduction-oxidation cycles (HO cycles) are also reflected in the electrochemical characteristics of the surface layer. As mentioned earlier, depending on the chemical composition of the Ni alloy substrate and the oxidising atmosphere, different types of oxides are observed in the scale: NiO, Al_2O_3 , Cr_2O_3 and TiO_2 . An XPS examination of the surface of the scale confirmed the presence of these oxides, with the exception of Al oxides, for the specimens of HY282-DMLS after 1 cycle (1HO) of hydrogenation and oxidation. Figure 9 shows

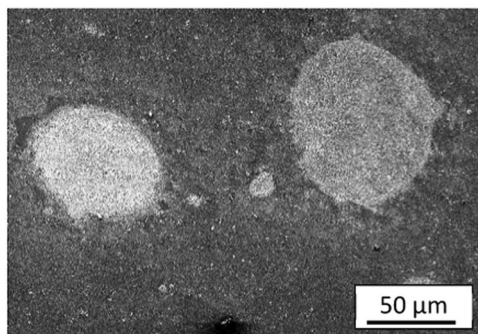


FIGURE 7 | Ni-Co precipitates on the surface morphology of an HY282 nickel alloy in its initial state after six hydrogenation/oxidation cycles (6 × HO). [Color figure can be viewed at wileyonlinelibrary.com]

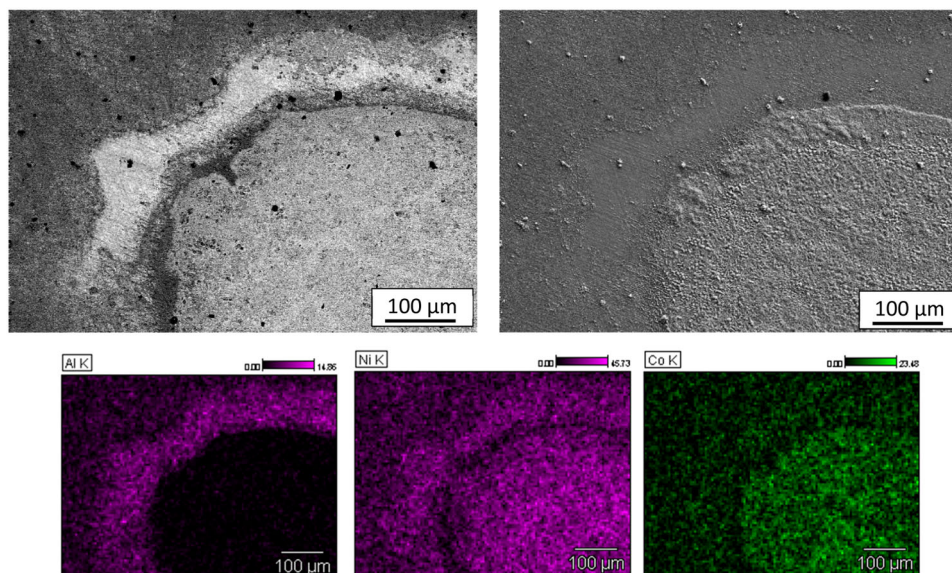


FIGURE 8 | Chemical analysis of Ni-Co precipitates formed on the oxide scale on HY 282 after six hydrogenation/oxidation cycles with element distribution illustrated through EDS maps. [Color figure can be viewed at wileyonlinelibrary.com]

typical XPS spectra of Cr2p (a), Ti2p (b) and Ni2p (c) recorded for the specimen after the 1HO oxidation/hydrogenation cycle.

Characterisation peaks were observed for chromium Cr_2O_3 (576.8 eV), CrO_3 (579.1 eV) and metallic Cr (574.8 eV). For titanium, the dominant peak refers to TiO_2 (458.7 eV). The occurrence of other nonstoichiometric titanium oxides was observed as follows: Ti_2O_3 (457.0 eV) and TiO_x (460.9 eV). The analysis of the XPS spectra showed the presence of the dominant oxide NiO (853.3 eV) and a lower signal from Ni_2O_3 (855.8 eV). The presence of other metal oxides and hydroxides, including Fe_2O_3 (710.4 eV), Fe_3O_4 (708.5 eV), MoO_2 (229.1 eV), MoO_3 (231.9 eV) and $\text{Co}(\text{OH})_2$ (781.5 eV) was also observed. They were derived from the alloying elements present in the HY282 alloy. The obtained XPS results also showed that Cr oxides constitute about 60% of all metal oxides, Ti oxides—about 30%, and about 10% are other oxides, including Ni oxides (~1%). Similar ranges of the binding energies of elements were determined for the specimen oxidised and hydrogenation six times at 750°C. After six cycles, no iron oxides were detected on the surface of the scale. However, Mo oxides (MoO_2 , MoO_3) and Co hydroxides and oxides ($\text{Co}(\text{OH})_2$, Co_3O_4) were observed, as in the case of the specimen oxidised once. The main difference observed between the oxidation cycles was that after six cycles, the contribution of Cr oxides was at about 50% and that of Ti oxides was about 40%. This means that the proportion of individual oxides changed due to the growth of the scale layer after successive oxidation cycles. Such behaviour led to notable changes in the corrosion resistance of the tested materials. The XRD test results, presented in Figure 10, confirm the change in the phase composition of the oxide scale during multiple oxidation–reduction cycles.

In the case of a single HO cycle, the oxide scale contains mainly chromium oxide Cr_2O_3 with a small admixture of titanium oxides TiO/TiO_2 . Extending the oxidation time results in a significant increase in the heterogeneity of the oxide scale, while its thickness increases (a decrease in the intensity of the peaks characterising the substrate is observed). The appearance

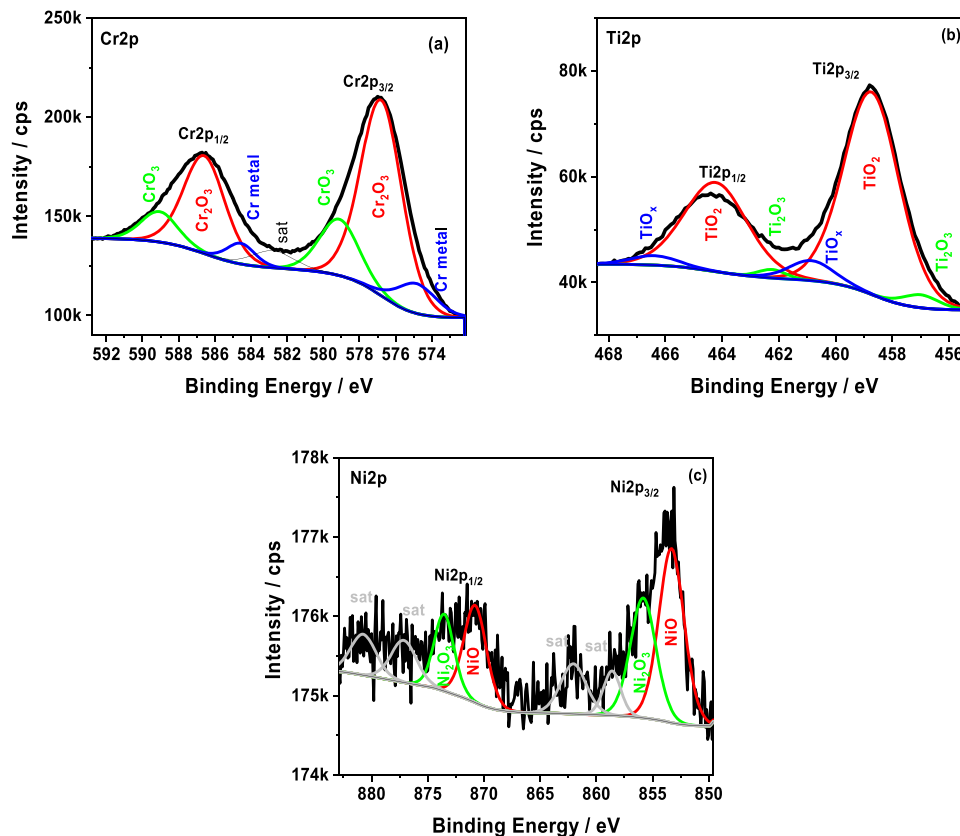


FIGURE 9 | High-resolution XPS spectra recorded on the HY282-DMLS specimen surface after one hydrogenation and oxidation cycle ($1 \times \text{HO}$). [Color figure can be viewed at wileyonlinelibrary.com]

of NiCr_2O_4 spinels in the oxide scale due to long-term oxidation of nickel alloys is consistent with the literature data [37]. Additionally, the increase in the size of NiCr_2O_4 precipitates (correlated with the increase in temperature and oxidation time) causes an increase in residual stresses in the oxide layer. It may lead to spallation of the scale and thus may be one of the reasons for the decreasing electrochemical resistance of HY282 observed in corrosion tests [37]. The presence of NiCr_2O_4 spinels in XRD studies and their absence in XPS studies indicates that the spinel is formed at the metal/oxide interface. Similar XRD spectra were obtained for the conventional HY282 alloy.

3.4 | Corrosion Test

Figures 11 and 12 show the impedance spectra of the conventional (HY282) (Figure 11) and Haynes 282-DMLS (Figure 12) after the first ($1 \times \text{HO}$) and last ($6 \times \text{HO}$) reduction-oxidation cycle in comparison to the HY282 in initial state after hydrogenation (1H) or after oxidation (1O).

An analysis of the spectra indicates an increase in the electrochemical nonhomogeneity of HY282 as a result of the formation of an oxide layer during the process of low-temperature oxidation, regardless of the initial microstructure (conventional or DMLS). The value of the ‘ n ’ parameter decreases with the increase in the number of reduction-oxidation cycles. A decrease in the value of the parameter ‘ n ’ in both states (DMLS—from $n = 0.74$ to $n = 0.58$, and conventional from $n = 0.85$ to $n = 0.61$) indicates an increase in the diffusion properties of the

layer. Although an increase in the thickness of the layer was observed, the scale tightness was reduced presumably due to hydrogen saturation. This allows the electrolyte to penetrate within the layer, thereby lowering the corrosion resistance of the nickel superalloy. Figure 13 summarises the values of charge transfer resistance through double layer (R_t resistance) of the conventional (HY282) and the DMLS (HY282–DMLS), showing the lower value in the case of 3D printing compared with the conventional Haynes 282 alloy.

An analysis of the changes in resistance (R_t) (Figure 13) indicates that hydrogenation has an adverse effect on the alloy’s corrosion resistance. Simultaneously, preliminary hydrogenation of the substrate enables the formation of oxide layers that have a higher resistivity than a single-oxidised substrate. A similar effect is obtained by cathodic sputtering during the preliminary stage of glow-discharge treatment, which facilitates the formation of nitrated or oxynitrated layers on steels [38] or NiTi alloys [39]. However, in multiple H-O cycles, the presence of thick surface layers with gradually more defects does not protect the substrate from corrosion processes occurring at the metal–oxide interface or from exfoliation of the oxide layer.

Figures 14 and 15 show the potentiodynamic curves of the conventional HY282 alloy (Figure 14) and the one produced by 3D printing (Figure 15). They confirm the presence of a passive layer, HY282’s susceptibility to pitting corrosion (conventional and DMLS), and the complexity of factors determining the corrosion resistance and durability of the scale layer formed during high-temperature oxidation.

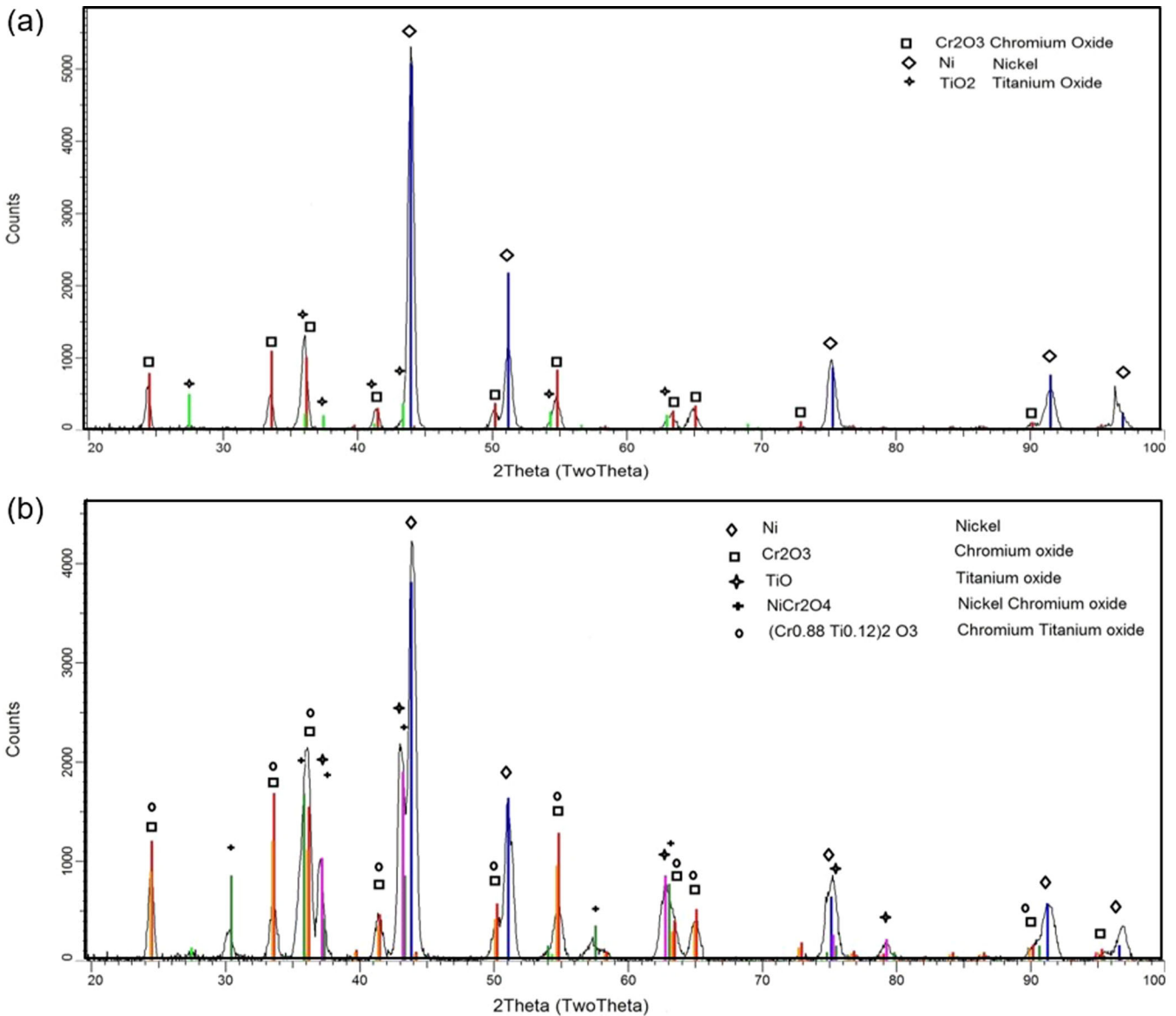


FIGURE 10 | XRD pattern of oxide scale from the surface of HY282-DMLS after various numbers of HO cycles. (a) after one cycle and (b) after six hydrogenation/oxidation cycles. [Color figure can be viewed at [wileyonlinelibrary.com](https://onlinelibrary.wiley.com)]

The shape of the potentiodynamic curves of the HY282 superalloy after the cathodic hydrogenation process indicates surface activation and the occurrence of a range of activation passivation due to the application of anodic polarisation. The durability of the hydrogenated passivation layer is similar to that of the initial material. The observed increase in the corrosion potential values (Table 2) of the hydrogenated material can be attributed to the etching of the most active areas and the exposure of the surface containing MC-type carbides rich in Ti-Mo. Short-term oxidation (24 h) causes an increase in corrosion resistance with minor ($\Delta E_{\text{corr}} = 100 \text{ mV}$) changes in corrosion potential. In addition, in the passive range the presence of two electrochemical processes associated with the formation of TiO_2 at grain boundaries and Cr_2O_3 on the surface of the alloy [22]. Short-term (24 h) oxidation of the hydrogenated substrate minimally reduces the corrosion potential, but the structural defects introduced accelerate oxidation and lead to an increase in corrosion resistance. Extending the oxidation time increases the corrosion potential (up to about 100 mV) due to the

increased share of titanium oxides in the scale. In the case of compact oxide layers, increasing their thickness reduces ion diffusion, thus, hindering the corrosion processes. Multiple saturating thick layers of scale with cathodic hydrogen causes a degradation of the scale, which intensifies corrosion processes. Increasing the polarisation intensity above $E > 800 \text{ mV}$ causes, according to Pourbaix diagrams, a change in the oxidation state of chromium compounds (from Cr^{+3} to Cr^{+6}), intensifying corrosion processes. Disturbance of the structure of the oxide scale initiates intense pitting corrosion shown in Figure 16.

The potentiodynamic studies of the HY282 superalloy produced using the DMLS technique (Figure 15) showed that the material is in the passive state and the increase in the value of current density is associated with the trans-passive area, which initiates pitting corrosion.

An analysis of the potentiodynamic curves indicates that the hydrogenation of Haynes 282 alloy has an adverse effect on its

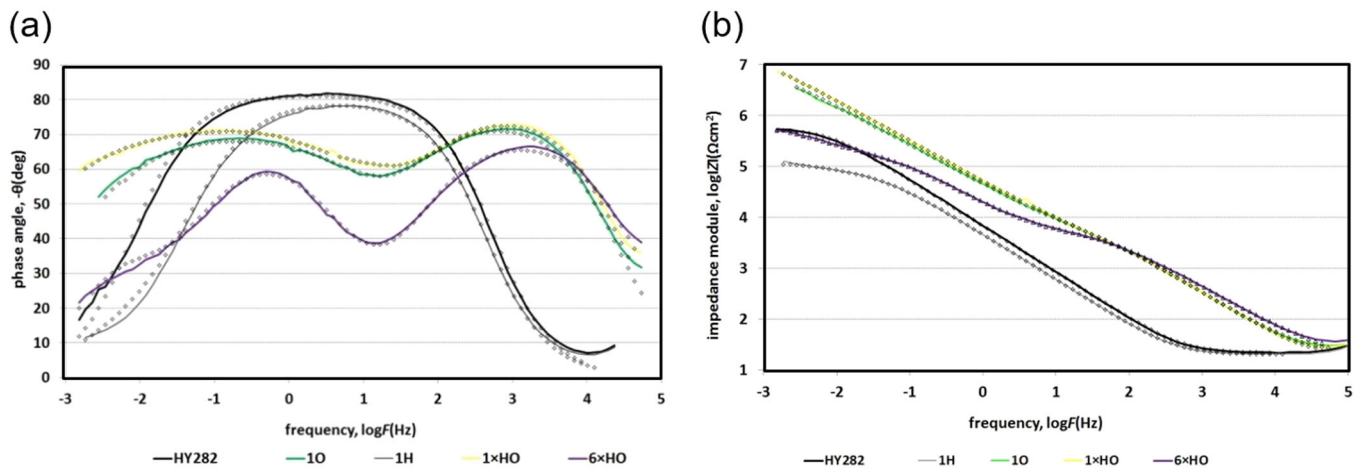


FIGURE 11 | Summary of the Bode plots of conventional HY282 nickel alloy in the initial state in subsequent reduction-oxidation cycles compared with the initial material (IS), after hydrogenation (1H) or after oxidation (1O); (a) phase angle plots and (b) impedance modulus plots. Solid line—date, dotted line—fit. [Color figure can be viewed at wileyonlinelibrary.com]

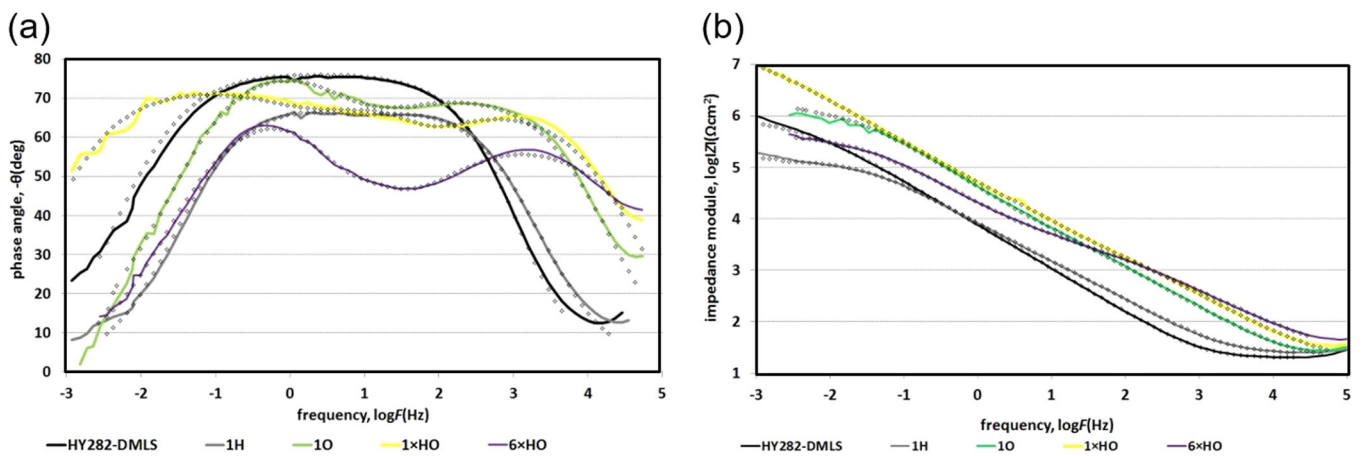


FIGURE 12 | Summary of the Bode plots of Haynes 282-DMLS nickel, in subsequent reduction-oxidation cycles compared with the initial material (IS), after hydrogenation (1H) or after oxidation (1O); (a) phase angle plots and (b) impedance modulus plots: solid line—date, dotted line—fit. [Color figure can be viewed at wileyonlinelibrary.com]

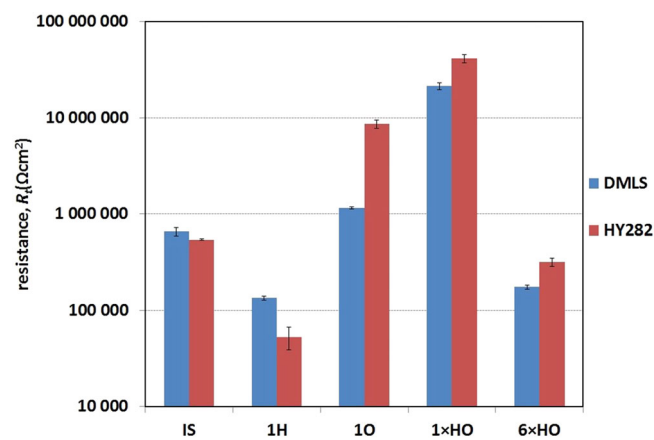


FIGURE 13 | Changes in the value of resistance (R_t)¹-in individual reduction-oxidation cycles (HO) for HY282 nickel alloy specimens in the initial state and produced using the DMLS technique compared with the initial material (IS) after hydrogenation (1H) or after oxidation (1O). 1 ÷ 6 × HO (number of cycles), H (hydrogenation), O (oxidation). [Color figure can be viewed at wileyonlinelibrary.com]

corrosion resistance. This is manifested by both, an increase in the density of corrosion currents and a decrease in the values of the corrosion potentials. It can be assumed that the observed differences in the values of the corrosion potentials of the hydrogenated materials (conventional and DMLS) are a result of the different responses of the substrate to hydrogen saturation. In the case of the DMLS material, high anisotropy facilitates the penetration of hydrogen and causes it to become trapped in the numerous dislocations characteristic of DMLS materials; this leads to a significant increase in electrochemical activity and facilitates isothermal oxidation [40].

4 | Summary

Depending on the reactive atmosphere and the chemical composition of the substrate, the composition of the oxide scale is different. In the case of the HY282 superalloy, research conducted by Pérez-González et al. [22] showed the presence of TiO_2 and Cr_2O_3 in the scale. Detailed studies [41] exposed the presence of a nanometric layer of titanium oxides on the surface and

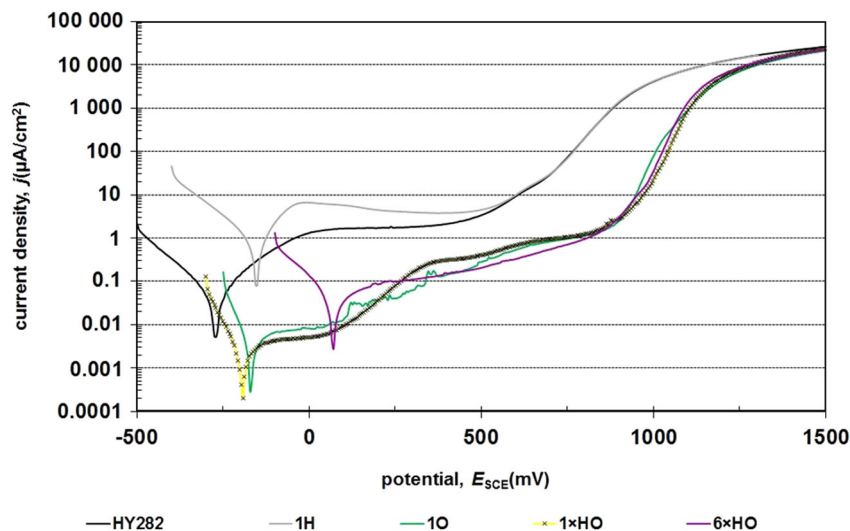


FIGURE 14 | Potentiodynamic curves of HY282 in selected H-O cycles, compared with the initial (HY282), hydrogenation (1H) or after oxidation (1O) material. [Color figure can be viewed at wileyonlinelibrary.com]

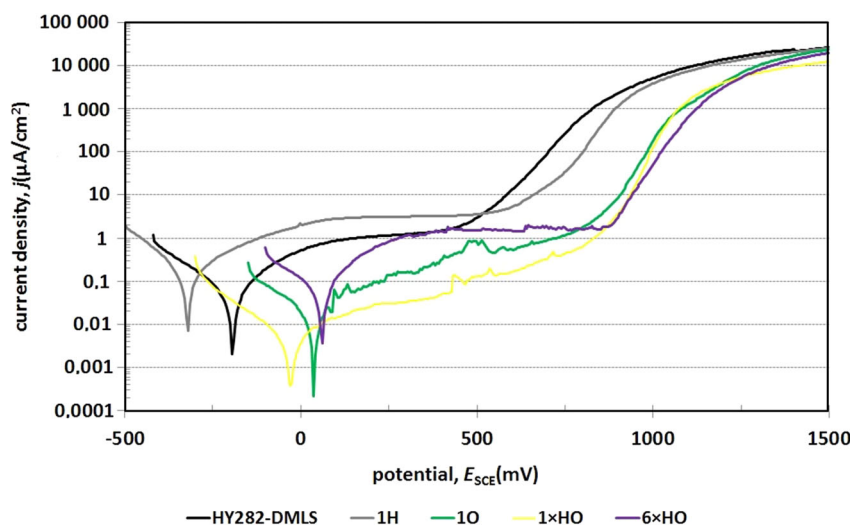


FIGURE 15 | Potentiodynamic curves of HY282 produced by the DMLS technique in individual H-O cycles, compared with the initial (HY282-DMLS), hydrogenation (1H) or after oxidation (1O) material. [Color figure can be viewed at wileyonlinelibrary.com]

TABLE 2 | Characteristic electrochemical values (potentiodynamic tests).

	HY282-DMLS		HY282 in the initial state	
	E_{corr} (mV)	i_{corr} ($\mu\text{A cm}^{-2}$)	E_{corr} (mV)	i_{corr} ($\mu\text{A cm}^{-2}$)
Without hydrogenation and oxidation (initial state)	-195	60.7×10^{-3}	-270	57.4×10^{-3}
Hydrogenation	-320	191.2×10^{-3}	-155	213.4×10^{-3}
Oxidation	30	25.8×10^{-3}	-170	2.9×10^{-3}
1 × HO	-25	6.1×10^{-3}	-190	1.8×10^{-3}
2 × HO	-5	5.7×10^{-3}	100	2.6×10^{-3}
3 × HO	40	3.3×10^{-3}	55	0.9×10^{-3}
4 × HO	20	9.5×10^{-3}	37	1.2×10^{-3}
5 × HO	70	16.5×10^{-3}	5	12.5×10^{-3}
6 × HO	60	88.2×10^{-3}	70	48.9×10^{-3}

Note: E_{corr} —corrosion potential, i_{corr} —corrosion current density.
 1 ÷ 6 × (number of cycles), H (hydrogenation), O (oxidation).

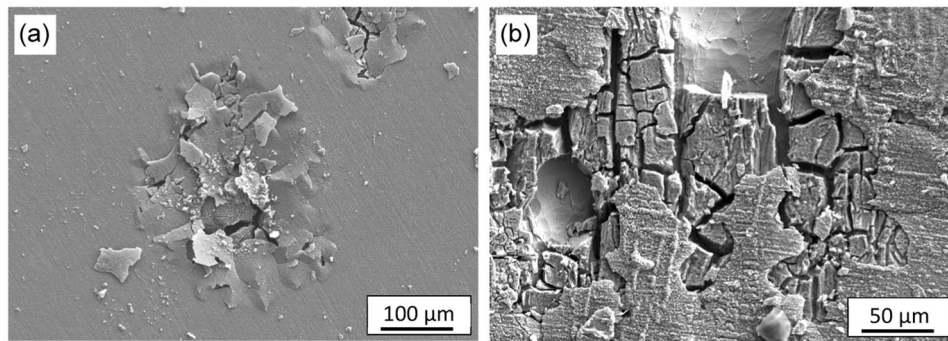


FIGURE 16 | Surface topography of the HY282 nickel alloy after six HO cycles and after potentiodynamic tests. (a) Conventional HY282 and (b) HY282-DMLS. [Color figure can be viewed at wileyonlinelibrary.com]

a layer of chromium oxides directly underneath it. This work confirmed that as the oxidation time increases, the proportion of TiO_2 in the scale increases. This is facilitated by the thermodynamic equilibrium favouring the formation of TiO_2 on the surface. One should highlight, that due to the small amounts of titanium in the alloy, the share of titanium oxides in the scale is insignificant. Young [42] suggests that in alloys containing chromium, the growth of TiO_2 oxides occurs mainly at grain boundaries. In the case of multiple oxidation/reduction cycles, the formation of NiCrO_4 spinels at the metal-oxide interface is observed. Their presence leads to an increase in electrochemical heterogeneity of the oxide scale. Oxidation of the HY282 alloy in air at 750°C additionally causes the process of internal oxidation of the reactive elements of the $\text{Ni}_3(\text{Al}, \text{Ti})$ phase, resulting in the formation of Al_2O_3 and TiO_2 oxides in the base material. In the case of conventional material, the thickness of the oxide layer increased with the increasing oxidation time, which is also confirmed by previous literature reports [18]. Different dependencies occur in the case of the oxidation of the substrate prepared using the DMLS technique. The thickness of the $\text{TiO}_2/\text{Cr}_2\text{O}_3$ scale is comparable during multiple H-O cycles, but a significant increase in the internal oxidation zone is observed. The constant thickness of the scale layer is probably caused by a different initial microstructure of the substrate—the material produced using the DMLS technique is characterised by a fine-crystalline structure containing dendrites and much greater porosity compared to the conventional material. The porosity of substrates after DMLS favours an increased internal oxidation zone, which may indirectly hinder the growth of the outer oxide scale layer, especially at relatively low oxidation temperatures. However, a thorough understanding of this phenomenon requires further detailed research.

One of the challenges facing nickel-based superalloys in high-hydrogen environments is their high susceptibility to hydrogen embrittlement. The high susceptibility of nickel superalloys to hydrogen can be limited by changing the microstructure [43] or their chemical composition, which affects the cohesion energy (increased cohesion energy by introducing boron, lanthanum and zirconium) [3]. It is known that the sensitivity to hydrogen and the number of intergranular cracks in nickel superalloys decreases with decreasing grain size, even though the hydrogen concentration in coarse-grained materials is lower than in fine-grained ones [3].

This is also confirmed by electrochemical tests of the initial materials (conventional and DMLS) after saturation with

cathodic hydrogen, showing an increase in the corrosion resistance of the material produced using the DMLS technology with a fine-crystalline structure compared to the conventional material with a coarse-grained structure.

5 | Conclusions

Based on the analysis of the test results, the following conclusions have been formulated:

1. Specimens of the HY282 nickel superalloy produced using the DMLS technique are characterised by a large internal oxidation zone and an improved resistance to hydrogenation as compared to HY282 nickel alloy in the initial state.
2. A comparison of the corrosion current density values between the specimens of conventional HY 282 nickel alloy and specimens produced using the DMLS technique indicates that the corrosion resistance of the 3D-produced materials is less than that of the conventional material, regardless of the oxidation time.

Acknowledgements

The research was funded by POB Technologie Materialowe of Warsaw University of Technology within the Excellence Initiative: Research University (IDUB) programme.

Conflicts of Interest

The authors declare no conflicts of interest.

Data Availability Statement

Data that support the findings of this study are available from the corresponding author upon reasonable request.

Endnotes

¹Rt—charge transfer resistance through double layer.

References

1. R. J. Smith, G. J. Lewi, and D. H. Yates, "Development and Application of Nickel Alloys in Aerospace Engineering," *Aircraft Engineering and Aerospace Technology* 73, no. 2 (2001): 138–147, <https://doi.org/10.1108/00022660110694995>.

2. T. M. Pollock and S. Tin, "Nickel-Based Superalloys for Advanced Turbine Engines: Chemistry, Microstructure, and Properties," *Journal of Propulsion and Power* 22 (2006): 361–374, <https://doi.org/10.2514/1.18239>.
3. A. I. Balitskii, Y. H. Kvasnytska, L. M. Ivaskevych, et al., "Hydrogen and Corrosion Resistance of Nickel Superalloys for Gas Turbines, Engines Cooled Blades," *Energies* 16, no. 3 (2023): 1154, <https://doi.org/10.3390/en16031154>.
4. T. Dudziak, L. Boron, M. Homa, et al., "The Influence of Fabrication Process on the Initial Stages of Steam Oxidation Performed on Haynes® 282® Alloy at 760°C," *Journal of Materials Engineering and Performance* 26 (2017): 239–249, <https://doi.org/10.1007/s11665-016-2417-5>.
5. S. Ban, Y. T. Shin, S. R. Lee, and H. Lee, "Corrosion Resistance of Inconel 625 Overlay Welded Inside Pipes as a Function of Heat Treatment Temperature," *International Journal of Electrochemical Science* 11 (2016): 7764–7774, <https://doi.org/10.20964/2016.09.22>.
6. L. O. Osoba, A. M. Oladoye, and V. E. Ogbonna, "Corrosion Evaluation of Superalloys Haynes 282 and Inconel 718 in Hydrochloric Acid," *Journal of Alloys and Compounds* 804 (2019): 376–384, <https://doi.org/10.1016/j.jallcom.2019.06.196>.
7. D. Kim, I. Sah, H. J. Lee, and C. Jang, "Hydrogen Effects on Oxidation Behaviors of Haynes 230 in High Temperature Steam Environments," *Solid State Ionics* 243 (2013): 1–7, <https://doi.org/10.1016/j.ssi.2013.04.010>.
8. X. Lu, A. Díaz, J. Ma, et al., "The Effect of Plastic Deformation on Hydrogen Diffusion in Nickel Alloy 625," *Scripta Materialia* 226 (2023): 115210, <https://doi.org/10.1016/j.scriptamat.2022.115210>.
9. M. Bruchhausen, B. Fischer, P. Hähner, and S. Soller, "Impact of High Pressure Hydrogen Atmosphere on the Mechanical Properties of Haynes 282 Superalloy," *Materials Testing* 54, no. 9 (2012): 612–618, <https://doi.org/10.3139/120.110365>.
10. Z. Liu, D. Zhao, P. Wang, et al., "Additive Manufacturing of Metals: Microstructure Evolution and Multistage Control," *Journal of Materials Science & Technology* 100 (2022): 224–236, <https://doi.org/10.1016/j.jmst.2021.06.011>.
11. A. Günen, U. Gürol, M. Koçak, and G. Çam, "A New Approach to Improve Some Properties of Wire Arc Additively Manufactured Stainless Steel Components: Simultaneous Homogenization and Boriding," *Surface and Coatings Technology* 460 (2023): 129395, <https://doi.org/10.1016/j.surfcoat.2023.129395>.
12. R. Sitek, J. Kaminski, B. Adamczyk Cieslak, et al., "Effect of Plasma Nitriding on Structure and Properties of Titanium Grade 2 Produced by Direct Metal Laser Sintering," *Metallography, Microstructure, and Analysis* 11 (2022): 852–863, <https://doi.org/10.1007/s13632-022-00903-5>.
13. R. Sitek, S. Puchlerska, I. Nejman, et al., "The Impact of Plastic Deformation on the Microstructure and Tensile Strength of Haynes 282 Nickel Superalloy Produced by DMLS and Casting," *Materials* 15, no. 21 (2022): 7545, <https://doi.org/10.3390/ma15217545>.
14. P. Fernandez-Zelaia, M. M. Kirka, S. N. Dryepontd, and M. N. Gushev, "Crystallographic Texture Control in Electron Beam Additive Manufacturing via Conductive Manipulation," *Materials & Design* 195 (2020): 109010, <https://doi.org/10.1016/j.matdes.2020.109010>.
15. A. S. Shaikh, F. Schulz, K. Minet-Lallemand, and E. Hryha, "Microstructure and Mechanical Properties of Haynes 282 Superalloy Produced by Laser Powder Bed Fusion," *Materials Today Communications* 26 (2021): 102038, <https://doi.org/10.1016/j.mtcomm.2021.102038>.
16. R. Ghiaasiaan, N. Ahmad, P. R. Gradl, S. Shao, and N. Shamsaei, "Additively Manufactured Haynes 282: Effect of Unimodal vs. Bimodal γ' - Microstructure on Mechanical Properties," *Materials Science and Engineering: A* 831 (2022): 142234, <https://doi.org/10.1016/j.msea.2021.142234>.
17. J. Boswell, J. Jones, N. Barnard, D. Clark, M. Whittaker, and R. Lancaster, "The Effects of Energy Density and Heat Treatment on the Microstructure and Mechanical Properties of Laser Additive Manufactured Haynes 282," *Materials & Design* 205 (2021): 109725, <https://doi.org/10.1016/j.matdes.2021.109725>.
18. R. N. Nnaji, M. A. Bodude, L. O. Osoba, O. S. I. Fayomi, and F. E. Ochulor, "Study on High-Temperature Oxidation Kinetics of Haynes 282 and Inconel 718 Nickel-Based Superalloys," *International Journal of Advanced Manufacturing Technology* 106 (2020): 1149–1160, <https://doi.org/10.1007/s00170-019-04290-0>.
19. Z. Liang and Q. Zhao, "High Temperature Oxidation of Fe–Ni-Base Alloy HR120 and Ni-Base Alloy HAYNES 282 in Steam," *Materials at High Temperatures* 36, no. 1 (2019): 87–96, <https://doi.org/10.1080/09603409.2018.1465712>.
20. F. A. Pérez-González, N. F. Garza-Montes-de Oca, and R. Colás, "High Temperature Oxidation of the Haynes 282® Nickel-Based Superalloy," *Oxidation of Metals* 82 (2014): 145–161, <https://doi.org/10.1007/s11085-014-9483-6>.
21. Z. Liang and Q. Zhao, "High Temperature Oxidation of Fe–Ni-Base Alloy HR120 and Ni-Base Alloy Haynes 282 in Steam," *Materials at High Temperatures* 36, no. 1 (2019): 87–96, <https://doi.org/10.1080/09603409.2018.1465712>.
22. F. A. Pérez-González, N. F. Garza-Montes-de Oca, and R. Colás, "High Temperature Oxidation of the Haynes 282® Nickel-Based Superalloy," *Oxidation of Metals* 82 (2014): 145–161, <https://doi.org/10.1007/s11085-014-9483-6>.
23. T. Dudziak, V. Deodeshmukh, L. Backert, et al., "High Temperature Corrosion Resistance of Advanced Engineering Materials Under Steam Oxidation Conditions for Ultra Super Critical (USC) Coal Power Plants," *EUROCORR* (2015): 1–10, <https://doi.org/10.13140/RG.2.1.2562.7762>.
24. A. Brittan, J. Mahaffey, and M. Anderson, "The Performance of Haynes 282 and Its Weld in Supercritical CO₂," *Materials Science and Engineering A* 759 (2019): 770–777, <https://doi.org/10.1016/j.msea.2019.05.080>.
25. Z. Liang, M. Yu, Y. Gui, and Q. Zhao, "Corrosion Behavior of Heat-Resistant Materials in High-Temperature Carbon Dioxide Environment," *JOM* 70 (2018): 1464–1470, <https://doi.org/10.1007/s11837-018-2975-0>.
26. S. Guo, D. Xu, G. Jiang, Z. Jing, S. Wang, and H. Lv, "High-Temperature Corrosion of Fe-Ni-Based Alloy HR6W, Ni-Based Alloys Haynes 282 and Inconel 740 in Supercritical Water at 450°C and 25 MPa," *Journal of Alloys and Compounds* 878 (2021): 160350, <https://doi.org/10.1016/j.jallcom.2021.160350>.
27. A. C. L. Kimmel, T. F. Malkowski, S. Griffiths, et al., "High-Temperature Corrosion of Inconel® Alloy 718, Haynes® 282® Alloy and CoWAlloy1&2 in Supercritical Ammonia/Ammonium Chloride Solution," *Journal of Crystal Growth* 498 (2018): 289–300, <https://doi.org/10.1016/j.jcrysgro.2018.06.018>.
28. Y. S. Ko, B. K. Kim, W. S. Jung, H. N. Han, and D. I. Kim, "Effect of the Microstructure of Haynes 282 Nickel-Based Superalloys on Oxidation Behavior Under Oxy-Fuel Combustion Conditions," *Corrosion Science* 198 (2022): 110110, <https://doi.org/10.1016/j.corsci.2022.110110>.
29. R. Sitek, K. Kulikowski, K. Paradowski, et al., "Influence of Ion Nitriding on Microstructure and Properties of Haynes 282 Nickel Superalloy Specimens Produced Using DMLS Technique," *Materials* 16 (2023): 5020, <https://doi.org/10.3390/ma16145020>.
30. K. Majchrowicz, Z. Pakieła, J. Kamiński, M. Płocińska, T. Kurzynowski, and E. Chlebus, "The Effect of Rhenium Addition on Microstructure and Corrosion Resistance of Inconel 718 Processed by Selective Laser Melting," *Metallurgical and Materials Transactions A* 49 (2018): 6479–6489, <https://doi.org/10.1007/s11661-018-4926-3>.
31. T. Dudziak, L. Boron, A. Gupta, et al., "Steam Oxidation Resistance and Performance of Newly Developed Coatings for Haynes® 282® Ni-Based Alloy," *Corrosion Science* 138 (2018): 326–339, <https://doi.org/10.1016/j.corsci.2018.04.005>.

32. W. J. Nowak, D. Serafin, and B. Wierzbka, "Effect of Surface Mechanical Treatment on the Oxidation Behavior of FeAl-Model Alloy," *Journal of Materials Science* 54 (2019): 9185–9196, <https://doi.org/10.1007/s10853-019-03509-5>.
33. P. Kofstad, *High Temperature Corrosion*, 2nd ed. (London, Canada, New York, NY, USA: Elsevier Applied Science Pub Co, 1988).
34. S. A. Bakar, N. Soltani, W. M. M. Yunus, E. Saion, and A. Bahrami, "Structural and Paramagnetic Behavior of Spinel NiCr₂O₄ Nanoparticles Synthesized by Thermal Treatment Method: Effect of Calcination Temperature," *Solid State Communications* 192 (2014): 15–19, <https://doi.org/10.1016/j.ssc.2014.05.002>.
35. M. Srivastava, V. Ezhil Selvi, V. K. William Grips, and K. S. Rajam, "Corrosion Resistance and Microstructure of Electrodeposited Nickel–Cobalt Alloy Coatings," *Surface and Coatings Technology* 201 (2006): 3051–3060, <https://doi.org/10.1016/j.surfcoat.2006.06.017>.
36. B. Bakhit, A. Akbari, F. Nasirpour, and M. G. Hosseini, "Corrosion Resistance of Ni–Co Alloy and Ni–Co/SiC Nanocomposite Coatings Electrodeposited by Sediment Codeposition Technique," *Applied Surface Science* 307 (2014): 351–359, <https://doi.org/10.1016/j.apsusc.2014.04.037>.
37. S. Voyshnis, A. Seyeux, S. Zanna, B. Martin-Cabanas, T. Couvant, and P. Marcus, "Oxide Layer Growth on Nickel-Base Alloy Surfaces in High Temperature Water and in O₂ Studied by Tof-Sims With Isotopic Tracers," *Corrosion Science* 145 (2018): 212–219, <https://doi.org/10.1016/j.corsci.2018.10.009>.
38. T. Borowski, K. Kulikowski, B. Adamczyk-Cieślak, K. Roźniatowski, M. Szychalski, and M. Tarnowski, "Influence of Nitrided and Nitrocarburised Layers on the Functional Properties of Nitrogen-Doped Soft Carbon-Based Coatings Deposited on 316L Steel Under DC Glow-Discharge Conditions," *Surface and Coatings Technology* 392 (2020): 125705, <https://doi.org/10.1016/j.surfcoat.2020.125705>.
39. J. Witkowska, J. Rudnicki, W. Piekoszewski, G. Raugh, J. Morgiel, and T. Wierzchoń, "Influence of Low Temperature Plasma Oxynitriding on the Mechanical Behavior of NiTi Shape Memory Alloys," *Vacuum* 156 (2018): 135–139, <https://doi.org/10.1016/j.vacuum.2018.07.027>.
40. M. Anand and A. K. Das, "Issues in Fabrication of 3D Components Through DMLS Technique: A Review," *Optics & Laser Technology* 139 (2021): 106914, <https://doi.org/10.1016/j.optlastec.2021.106914>.
41. P. Gore, O. P. Gosain, M. P. Singh, B. Basu, and K. Chattopadhyay, "Towards Understanding the Oxide Evolution in Inconel 740H and Haynes 282 in Ambient Pressure Steam Oxidation," *Oxidation of Metals* 97 (2022): 509–525, <https://doi.org/10.1007/s11085-022-10103-9>.
42. D. Young, *High Temperature Oxidation and Corrosion of Metals* (Amsterdam: Elsevier Corrosion Series, 2008).
43. Z. Zhang, K. L. Moore, G. McMahon, R. Morana, and M. Preuss, "On the Role of Precipitates in Hydrogen Trapping and Hydrogen Embrittlement of a Nickel-Based Superalloy," *Corrosion Science* 146 (2019): 58–69, <https://doi.org/10.1016/j.corsci.2018.10.019>.